



Magnetic and electrical properties of Ni-doped $\text{Ba}(\text{Ti}_{0.8}\text{Zr}_{0.2})\text{O}_3$ materials

N. H. Thoan¹ · C. T. T. Trang¹ · N. D. Co² · P. V. Vinh³ · N. N. Trung¹ · L. H. Bac¹ · H. M. Tuan¹ · N. Q. Huy¹ · D. D. Dung¹ 

Received: 26 April 2021 / Accepted: 18 June 2021 / Published online: 28 June 2021
© The Author(s), under exclusive licence to Springer-Verlag GmbH, DE part of Springer Nature 2021

Abstract

In this work, Ni-doped lead-free ferroelectric $\text{Ba}(\text{Ti}_{0.8}\text{Zr}_{0.2})\text{O}_3$ materials were well synthesized by a simple chemical route. The complex magnetic behavior of the materials was explained by the random distribution of Ni cations into the $\text{Ba}(\text{Ti}_{0.8}\text{Zr}_{0.2})\text{O}_3$ host lattice. As increasing the Ni concentration to 9 mol%, nonlinear electric polarization behavior remained unchanged in the $\text{Ba}(\text{Ti}_{0.8}\text{Zr}_{0.2})\text{O}_3$ materials. The observations in nonlinear magnetization and electric polarization in Ni-doped $\text{Ba}(\text{Ti}_{0.8}\text{Zr}_{0.2})\text{O}_3$ materials suggested an extension of new material functions to the development of advanced materials for electronic devices.

Keywords BaZrO_3 · BaTiO_3 · Lead-free ferroelectric · Ferromagnetic · Ni dopants

1 Introduction

Common ferroelectric $\text{Pb}(\text{Zr},\text{Ti})\text{O}_3$ -based (PZT) ceramic materials have been widely applied in electronic devices [1]. However, the current environment and human health are affected because these materials contained a considerable amount of Pb (~60 wt.%) [1]. Lead-based ferroelectric materials are toxic to the human body and damage the environment [1, 2]. It is thus necessary to develop a new type of lead-free ferroelectric materials to replace the PZT in current electronic devices. Among the lead-free ferroelectric materials, BaTiO_3 -based materials such as $(\text{Sr},\text{Ba})\text{TiO}_3$ are developed, which could replace PZT-based materials in electronic devices, such as dynamic random access memories, ferroelectric random access memory, capacitors, or microwave components [3–7]. However, the unstable phase of Sr modified at the Ba site in BaTiO_3 materials is a challenge in

research because the radius of Sr cations is smaller than that of Ba cations, resulting in local chemical compression. The hopping of electrons between Ti^{3+} and Ti^{4+} cations became easier when the distance between Ti^{3+} and Ti^{4+} cations was closer via chemical strain. As a result, the leakage current of Sr-modified BaTiO_3 materials increased, larger than that of BaTiO_3 materials [3]. Note that the Ti^{3+} defects existed in BaTiO_3 -based materials because oxygen vacancies promoted the reduction in the valence state of Ti^{4+} . Recently, the leakage current issue in $(\text{Ba},\text{Sr})\text{TiO}_3$ materials is addressed by Zr impurities as a substitute for Ti sites [3, 8–11]. Bada-panda et al. reported that Zr-modified BaTiO_3 compounds existed in more stable phases than Sr-modified BaTiO_3 compounds [3]. In addition, Bootchanont et al. reported that the Ti off-center displacements were dependent on the Zr concentration-doped BaTiO_3 materials [8]. The $\text{Ba}(\text{Ti}_{1-x}\text{Zr}_x)\text{O}_3$ compounds exhibited traditional ferroelectric behaviors for x smaller than 10 mol%, whereas a typical relaxor ferroelectric behavior for x exhibited in the range of 0.26–0.4 [9, 10]. Yu et al. reported that the large unipolar strain levels of 0.18–0.25% and the remanent polarization of 13–18 $\mu\text{C}/\text{cm}^2$ were obtained for BaZrO_3 -modified BaTiO_3 with BaZrO_3 dopants ranging from 3 to 8 mol% [11]. Mahajan et al. reported that the BaZrO_3 solid solution into the host BaTiO_3 with 15 mol% increased the dielectric constant from 1675 to 10,580 at room temperature (RT), whereas the maxima dielectric constant value increased from ~13,626 to 21,023 with diffuse phase transition compared with pure

✉ D. D. Dung
dung.dangduc@hust.edu.vn

¹ Multifunctional Ferroics Materials Lab., School of Engineering Physics, Ha Noi University of Science and Technology, 1 Dai Co Viet road, Hanoi, Vietnam

² Faculty of Engineering Physics and Nanotechnology, VNU University of Engineering and Technology, Vietnam National University, 144 Xuan Thuy road, Hanoi, Vietnam

³ Faculty of Physics, Hanoi National University of Education, 136 Xuan Thuy road, Hanoi, Vietnam

BaTiO₃ [12]. Huang et al. reported an improvement in charge trapping in nonvolatile memory based on Zr-doped BaTiO₃ materials [13]. Therefore, the Ba(Ti,Zr)O₃ system can be used to replace PZT-based materials in currently used electronic devices. According to Bera et al. and Yu et al., (1-*x*)BaTiO₃ + *x*BaZrO₃ compounds with *x* < 0.1 showed traditional ferroelectric behavior, while the similar systems with *x* the range 0.26–0.4 showed a typical relaxor ferroelectric behavior [9, 10]. Yu et al. also reported that a large unipolar strain level of 0.18–0.25% was obtained in that BaZrO₃-modified BaTiO₃ materials with 0.03–0.08 mol% of BaZrO₃, while the remnant polarization was estimated at 13–18 μC/cm² [11]. Liu et al. reported that the normal ferroelectric properties of BaTiO₃ could change to relaxors by adding BaZrO₃ with high concentration levels up to 40 mol% [14]. The main problem was that the solid-state reaction method to synthesize the BaTiO₃-BaZrO₃ system required too high sintering temperatures up to 1300 °C onwards [9]. The reduction in sintering temperatures for synthesizing BaTiO₃-BaZrO₃ systems was achieved by using a sol-gel method where the phase forming could start from 400 °C [15]. Among a wide range of Ba(Ti,Zr)O₃ systems, Ba(Ti_{0.8}Zr_{0.2})O₃ materials show continuous conductance change for both increasing and decreasing and good potential for resistive switching memory devices (memristors or ReRAM), indicating that the synaptic weight change is responsible for the biological learning process as artificial synapses in the neuromorphic systems [16]. Therefore, injecting ferromagnetism in current lead-free ferroelectric Ba(Ti_{0.8}Zr_{0.2})O₃ compounds is interesting for the extension of function materials for smart electronic applications.

Recently, doping transition metals into host lead-free ferroelectric materials is a potential method for creating a new material type that exhibited ferroelectric and ferromagnetism for smart electronic devices [17–19]. Therefore, novel functions of lead-free ferroelectric materials are studied by combining them with ferromagnetism at room temperature. Room temperature ferromagnetism (RTF) in lead-free ferroelectric materials has been reported for Fe-, Co-, Ni-, Mn-, and Cr-doped Bi_{0.5}Na_{0.5}TiO₃ materials [20–24]. RTF in Bi_{0.5}K_{0.5}TiO₃ materials is also achieved via doping transition metals, such as Fe, Co, Mn, Ni, and Cr [25–29]. RTF is reported for Co-, Fe-, and Mn-doped KNbO₃ samples [30–33]. Tiwari et al. reported that diamagnetic properties were exhibited in Ba- and Sc-co-doped KNbO₃ materials [34]. In addition, ferromagnetic ordering at RT is reported for various BaTiO₃ materials doped with transition metals, including Fe, Co, Ni, Mn, and Cr [35–39]. The observation in the ferromagnetic state of transition metal-doped lead-free ferroelectric materials is important in creating a new type of electronic devices, such as a four-state multiferroic memory [40]. The Ba(Ti_{0.8}Zr_{0.2})TiO₃ composition shows good electrical properties among a wide range of Ba(Ti,Zr)O₃-based

compositions [14, 41, 42]. Recently, there is the observation in complex ferromagnetism at room temperature in Fe-, Mn-, and Co-doped Ba(Ti_{0.8}Zr_{0.2})O₃ materials [43–45]. In addition, the room temperature ferromagnetism was obtained in various Ni-doped lead-free ferroelectric materials such as Bi_{1/2}Na_{1/2}TiO₃, Bi_{1/2}K_{1/2}TiO₃, BaTiO₃ materials [22, 28, 37]. However, so far, there was no report on the influence of Ni impurity-doped Ba(Ti_{0.8}Zr_{0.2})O₃ materials on the optical, magnetic, and electrical properties.

In this work, the Ni-doped Ba(Ti_{0.8}Zr_{0.2})TiO₃ compounds are fabricated by a simple chemical route method. The complex random incorporation of Ni into the Ba(Ti_{0.8}Zr_{0.2})TiO₃ host lattice enhances the magnetic properties of host materials. We obtained the nonlinear electric polarization of Ba(Ti_{0.8}Zr_{0.2})TiO₃ materials by incorporating Ni impurities into the host lattice.

2 Experimental

Ba(Ti_{0.8}Zr_{0.2})O₃ and Ni-doped Ba(Ti_{0.8}Zr_{0.2})O₃ materials with 0.5, 1, 3, 5, 7, and 9 mol% Ni (namely BZT and BZT-*x*Ni with *x* = 0.5–9, respectively) were synthesized by a chemical route method. Precursors included barium carbonate BaCO₃, tetraisopropoxytitanium IV C₁₂H₂₈O₄Ti, ZrO(NO₃)₂·*x*H₂O, and Ni(NO₃)₂·6H₂O. The solvents used in this study included acetic acid, acetylacetone, and de-ionized water. Firstly, raw BaCO₃ was weighed and dissolved in a mixed solution of acetic acid and de-ionized water at the volume ratio of 1:5. Secondly, ZrO(NO₃)₂·*x*H₂O and Ni(NO₃)₂·6H₂O were weighed as an estimation of doping levels and then added to the solutions. After 2–3 h of magnetic stirring, homogeneous transparent solutions were obtained. Subsequently, consistent amounts of the C₁₂H₂₈O₄Ti solution were reduced in the later solutions. After 5 h of magnetic stirring, homogeneous sols were formed from the final solutions. The sols were then left in an oval at 100 °C to obtain dry gels. The dry gels were annealed at 900 °C in the air for 3 h, then naturally cooled to room temperature, and ground to form powder samples. The chemical composition of the samples was measured by energy-dispersive X-ray spectroscopy (EDX, S-4800 Hitachi) and further confirmed by using an electron probe microanalyzer (EPMA, Shimadzu EPMA 1600). The surface morphologies of pure BZT and Ni-doped BZT compounds were achieved by field-emission scanning electron microscopy (FE-SEM, S-4800 Hitachi). The crystal structures of the samples were detected by X-ray diffraction (XRD, Bruker D8 Advance) spectroscopy. Raman measurements were carried out at room temperature using a Renishaw in Via Micro Raman Microscope system (Renishaw plc.) equipped with a 633-nm laser. Ultraviolet–visible (UV–Vis, Jasco V-670) absorption spectroscopy measurements were carried out to characterize

the optical properties of the samples. The magnetic properties of pure BZT and Ni-doped BZT compounds at RT were obtained by using a vibrating sample magnetometer (VSM, Lakeshore 7404). Each powder sample was mixed with 5 wt.% polyvinyl alcohol as a binder and pressed into a disk pellet at 98 MPa by using a 24-Ton pellet presser (MP24A, Across International) with cylindrical dies $\phi = 6$ mm. The pellets were sintered at 1100 °C for 3 h in the air and then naturally cooled to RT. The pellet's surface was polished and covered by silver paste, and then thermally treated at 700 °C for 30 min in the air. Electrical measurements were conducted by a Precision LC II ferroelectric test system (Radiant Technologies Inc.) and an HP 4192A LF impedance analyzer.

3 Results and discussions

The appearance of expected chemical compositions in the pure BZT compound was qualified by using EDX spectrum, as shown in Fig. 1a. All expectation chemical elements, including Ba, Ti, and O, appeared in the EDX spectrum by indexing the typical emission energy. As shown in Fig. 1b, the impurity Ni elements were clearly observed in the EDX spectrum of 9 mol% Ni-doped BZT materials. The result confirmed the presence of Ni cations in the as-prepared samples. The quality EDX results showed direct evidence for the presence of all expected chemical elements in both pure BZT and Ni-doped BZT samples.

The FE-SEM images in Fig. 2 showed the influence of Ni concentration on the surface morphology of BZT samples. The inset of each figure showed the size distribution of frequent particles. The distribution of pure BZT material exhibited homogeneous surface morphologies in Fig. 2a. The grain size of pure BZT material was estimated at approximately 50–80 nm. Figure 2b–g shows the surface morphologies of the Ni-doped BZT samples with various Ni concentrations in the range of 0.5–9 mol%, exhibiting an inhomogeneous grain size distribution. As shown in Fig. 2g, the grain size of the 9 mol% Ni-doped BZT sample decreased to approximately 10–30 nm. The complex grain growth of BZT materials concerning Ni concentrations could be explained by two main mechanisms associated with oxygen vacancies and impurities. In general, oxygen vacancies promoted grain growth, whereas impurities hindered grain growth [46–49]. Oxygen vacancies were natural defects and possibly enhanced by substituting Ni^{2+/3+} for Ti⁴⁺ to balance valence states in oxide materials. By contrast, increased levels of Ni impurity hindered grain growth, thereby leading to an inhomogeneous distribution of grain size. As a result, the compensative interaction of oxygen vacancies and impurities during phase formation resulted in the inhomogeneous distribution of grain size.

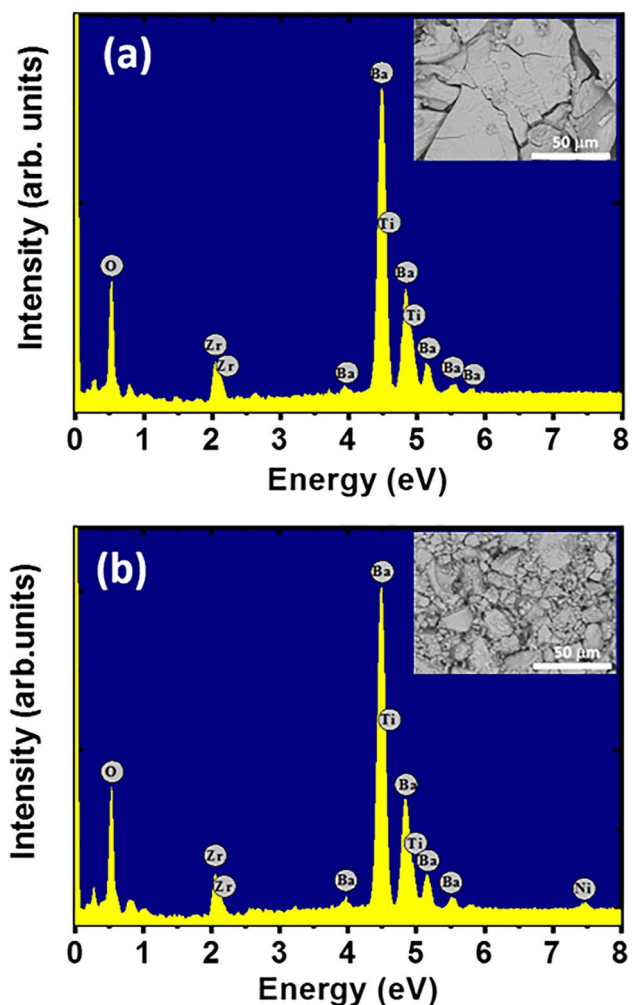


Fig. 1 Energy-dispersive X-ray, EDX, spectra of **a** pure BZT and **b** 9 mol% Ni-doped BZT samples. The inset of each figure shows a selected area for chemical composition measurements, respectively

To better understand the role of Ni doping on the structure of the studied samples, XRD measurements were performed. XRD patterns of pure BZT and BZT-xNi samples in Fig. 3a revealed the influence of Ni doping on the host BZT lattice. Based on the XRD peak positions and their relative intensity, all studied samples were assigned to a tetragonal crystal structure (P4mm symmetry). No additional peak related to either Ni impurity or phase separation was observed in the XRD patterns of Ni-doped BZT samples, indicating that the structure of Ni-doped BZT remains unchanged after Ni doping. This observation confirmed the random incorporation of Ni impurities into the host BZT lattice. The incorporation of Ni into the BZT lattice via Ni cation substitution is illustrated in Fig. 3b, where the XRD patterns of pure BZT and Ni-doped BZT samples were enlarged from 30.0° to 32.5° for satellite peaks (101)/(110). As shown in Fig. 3b, the peak around 31.2° shifted to higher angles as increasing Ni

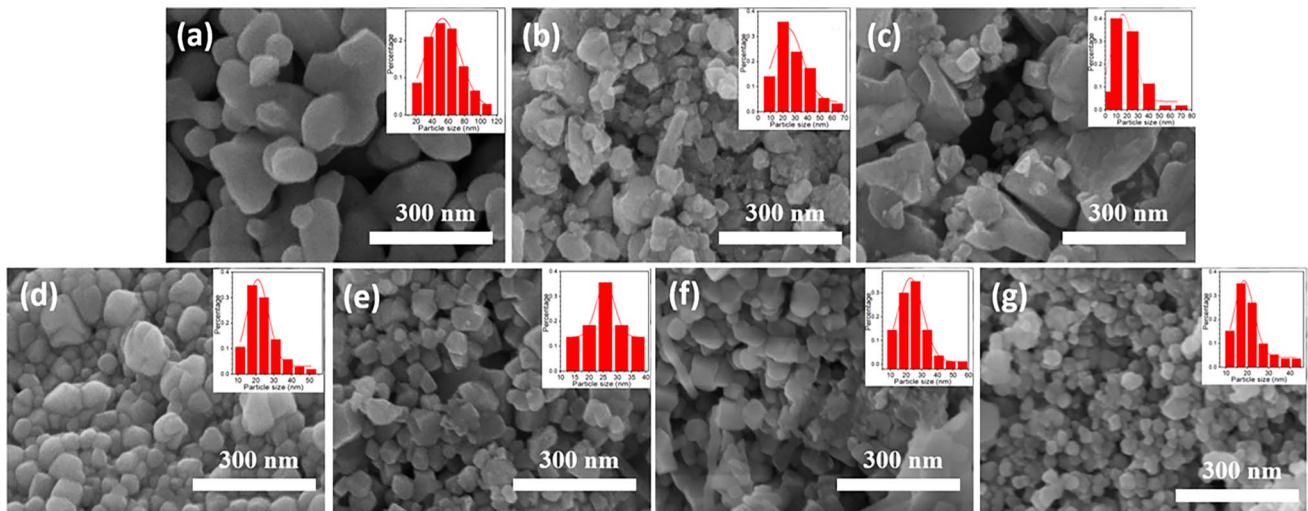
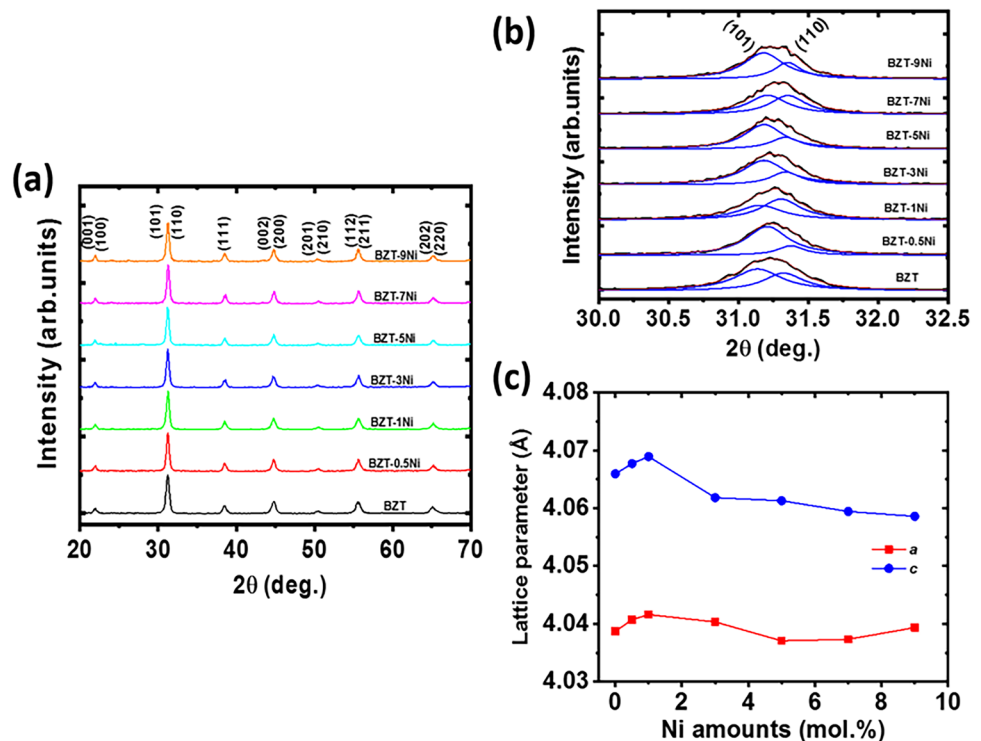


Fig. 2 Field-emission scanning electron microscopy (FE-SEM) images **a** pure BZT and Ni-doped BZT samples with **b** 0.5, **c** 1, **d** 3, **e** 5, **f** 7, and **g** 9 mol%. The inset of each figure shows the size distribution of frequent particles

Fig. 3 **a** X-ray diffraction patterns, **b** magnification of X-ray patterns in the 2θ range of $30.0\text{--}32.5^\circ$, and **c** lattice constants (a , c) of pure BZT and Ni-doped BZT with 0.5, 1, 3, 5, 7, and 9 mol%



concentrations, indicating compression of lattice parameters in our studied samples. Furthermore, the lattice parameters a and c of the pure BZT and the Ni-doped BZT according to Ni doping level are shown in Fig. 3c. The results show that distorted lattice parameters of BZT compound are not linear as a function of Ni doping amounts, which has complexed distortion in lattice parameters. The lattice distortion of the Ni-modified BZT compounds could be understood by considering the radii of the impurity cations and the

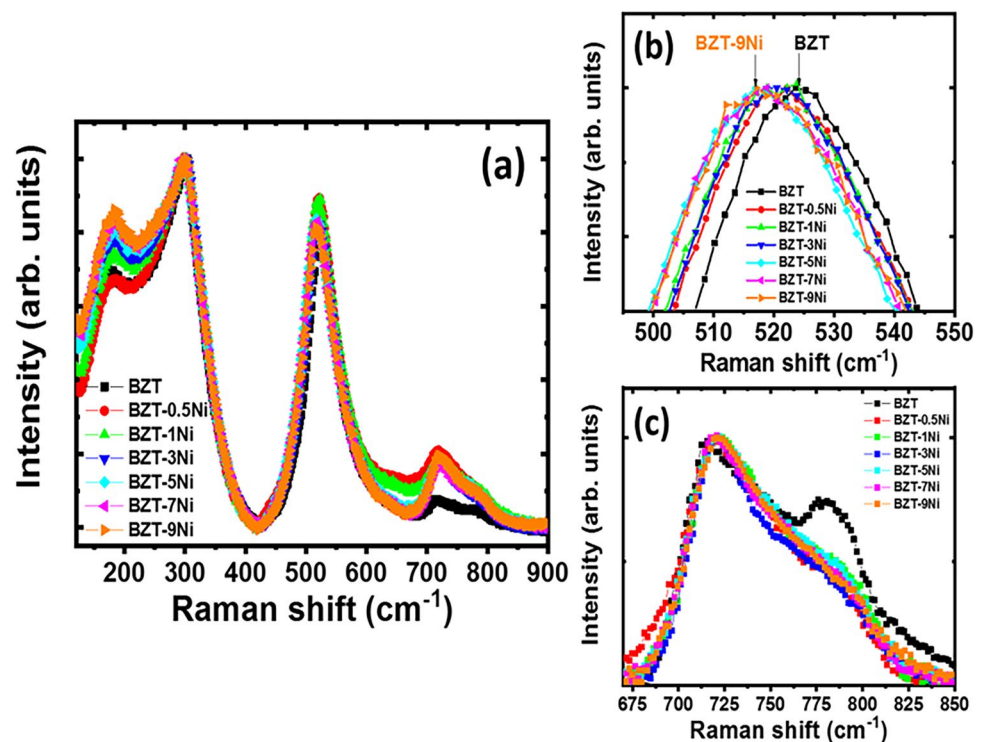
host cations. Shannon reported that the sizes of Ti^{4+} and Zr^{4+} cations in the coordination number (CN) of VI were 0.605 and 0.72 Å, respectively [50]. However, the size of Ni cations was complex, depending on their valence and spin states [50]. At the CN of VI, the radius of Ni^{2+} cations was 0.690 Å [50]. Having the same CN of VI, Ni^{3+} cations had a radius of 0.56 and 0.60 Å for the lower spin and high spin states, respectively, whereas Ni^{4+} cations had a radius of 0.48 Å at the low spin state [50]. Consequently, the complex

local lattice distortion can be obtained by randomly incorporating Ni cations into Ti or Zr sites in BZT compounds. The same trend of lattice compression was expected when the Ni³⁺ cations with either low spin or high spin states and the Ni⁴⁺ cations incorporated into the Ti sites because the radius of the Ni^{3+/4+} cations was smaller than that of the Ti⁴⁺ cations. However, the lattice parameters of BZT compounds might be expanded when Ni²⁺ was incorporated on the Ti sites. In addition, the oxygen vacancies were created by random incorporation of Ni²⁺ and Ni³⁺ cations for the Ti⁴⁺ or Zr⁴⁺ site to maintain charge neutrality. Notably, the size of oxide vacancies in perovskite-structured oxides was 1.31 Å, which was lower than that of oxygen anion (1.4 Å) [51]. So, the random presence of oxygen vacancies in the host lattice caused the lattice parameter to shrink. The relationship of lattice parameter compressing via oxygen vacancies and transition metal dopants was reported in Refs. [22, 24, 28, 29]. Recently, Chen et al. reported that the Ni cations possibly filled at the A sites in perovskite lead-free ferroelectric Bi_{0.5}Na_{0.5}TiO₃ materials [52]. Shannon reported that the radius of the Ba²⁺ cations was 1.60 Å, which was larger than that of Ni²⁺ cations [50]. Consequently, the substitution of Ni²⁺ at the A site of the BZT compounds resulted in the compression of lattice parameters. So far, the origin of lattice distortion in the host BZT materials via Ni dopants was not clear, needing further investigation to stop the incorporation of the Ni valence and spin states with host BZT compounds. Moreover, the compensation of the preferred site for the substitution of Ni cations in the host BZT lattices should

be confirmed. However, Ni-induced lattice distortion was important for the random incorporation of Ni cations into the host BZT materials. Furthermore, the average crystalline size of pure BZT and Ni-doped BZT samples was estimated using the Scherrer equation $D_{hkl} = k\lambda/\beta_{hkl}\cos\theta$, where D_{hkl} is the crystallite size in the direction perpendicular to the lattice planes, (hkl) are the Miller indices of the planes being analyzed, k is a numerical factor frequently referred to as the crystallite-shape factor, λ is the X-ray wavelength, β_{hkl} is the width (full-width at half-maximum) of the X-ray diffraction peak in radians, and θ is the Bragg angle [53, 54]. In our calculation method, we used k factor of approximately 0.9 [54, 55]. In our experimental, the Cu K_{α} with a radiation wavelength of 1.5406 Å was used as X-ray sources for characterization of crystal Ni-doped BZT phase. The pure BZT materials exhibited an average crystalline size of around 16 nm. The addition of Ni impurities into host BZT materials resulted in a slight increase in the average crystalline size in the range from 18 to 20 nm. Our observation of average crystalline sizes from XRD spectra was well consistent with obtained results from surface morphology FE-SEM.

The role of random incorporation of Ni impurity cations into host BZT materials would be further confirmed by using Raman scattering studies. Figure 4a shows the Raman spectra of the pure BZT and Ni-doped BZT samples measured at room temperature. For the pure BZT sample, the Raman spectrum could be divided into three main regions within the wavenumber range of 150–900 cm⁻¹. That shape of Raman spectra remained unchanged after Ni doping with

Fig. 4 a Raman spectra at room temperature of the pure BZT and Ni-doped BZT as a function of Ni amounts, and the magnified Raman spectra in the wavenumber range of **b** 480–550 cm⁻¹ and **c** 670 to 850 cm⁻¹

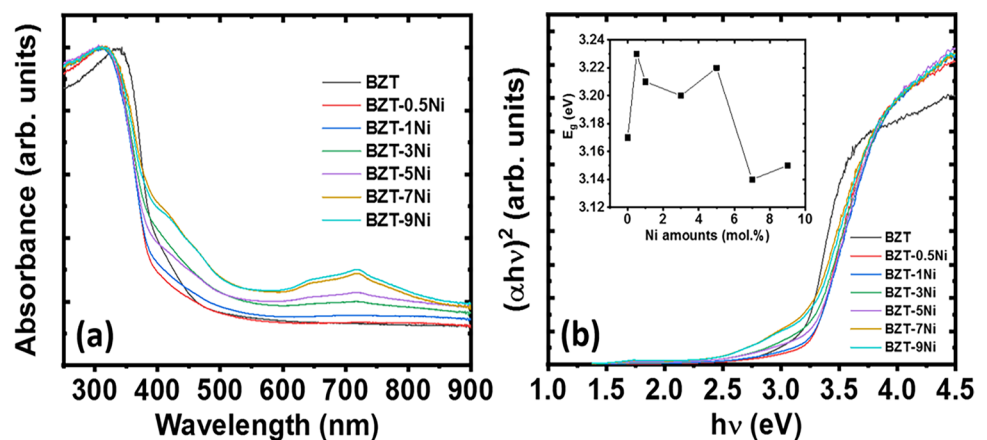


up to 9 mol%, which further confirmed that no impurity-related phase was appeared, with well consistent with the XRD results. The observation of the main peaks around 302 cm^{-1} and broad peaks at around 715 cm^{-1} along with other peaks also further confirmed the characteristic of tetragonal structural of studied samples with XRD results [56, 57]. It was suggested that Raman active modes of the tetragonal structure BZT compounds followed the tetragonal BaTiO_3 structure, consisting of $4E(\text{TO} + \text{LO}) + 3A_1(\text{TO} + \text{LO}) + B_1(\text{TO} + \text{LO})$ modes [56]. The observed anti-resonance effect at 175 cm^{-1} was assigned to a coupling between the sharp $A_1(\text{TO}1)$ and broad $A_1(\text{TO}2)$ modes [56, 58]. Singh et al. reported that the vibration Raman peaks around 270 and 304 cm^{-1} were caused by the vibration of TiO_6 group, while the peaks at approximately 514 cm^{-1} were related to the vibration displacement of oxygen atoms [59]. The influence of oxygen vacancies on the active vibration modes in BZT materials via Ni doping is shown in Fig. 4b. The center broad peaks around 523 cm^{-1} of pure BZT materials tended to shift to a lower wavenumber, about 517 cm^{-1} , as increasing the Ni impurity amount up to 9 mol%, which were suggested to be related to the oxygen vacancies [60]. Note that the oxygen vacancies were created due to the difference in valence states of $\text{Ni}^{2+/3+}$ cations that were randomly incorporated at the Ti sites in the host BZT materials. The evidence of vacancy defects in the BZT lattices via Ni doping was well consistent with the XRD results where BZT lattice parameters were compressed after incorporating Ni cations into the BZT host lattices. Vinothini et al. reported that the mode at around 715 cm^{-1} is a mixed A_1 and E modes associated with the breathing of BO_6 octahedra in the ferroelectric phase, whereas the mode at around 780 cm^{-1} is a stretching mode of BO_6 octahedral related to A - or B -site substitutions in the perovskite structure [61]. The $E_1(\text{TO}1)$ and $E_1(\text{TO}2)$ modes associated with the tetragonal–cubic phase transition were observed at 116 and 301 cm^{-1} , respectively, whereas the $A_1(\text{LO}3)$ mode was found at 720 cm^{-1} , with zirconium (Zr) substituted at the titanium (Ti) sites. However, the

coupling between the sharp $A_1(\text{TO}1)$ and broad $A_1(\text{TO}2)$ modes decreases as the intensity of the $A_1(\text{TO}2)$ mode decreases [62, 63]. In addition, the peaks at 720 cm^{-1} could be labeled as mixed A_1 and E mode associated with the breathing mode of BO_6 octahedra in the ferroelectric phase, whereas the peaks at 789 cm^{-1} can be labeled as stretching modes (A_1g asymmetric breathing) mode of BO_6 octahedra related to Zr substitution at Ti lattice sites [64, 65]. Figure 4c shows the magnified Raman spectra of the pure BZT and Ni-doped BZT materials in the wavenumber range from 670 to 850 cm^{-1} . Two Raman peaks were observed at around 717 cm^{-1} and 787 cm^{-1} which were well consistent with the recent observation in BZT materials [61, 62, 64, 66]. Our results showed that the intensity of the Raman peak at around 787 cm^{-1} decreased after randomly incorporating Ni cations into the host BZT lattices, that being suggested to relate to Ni substitution at Ti lattice sites.

The Ni doping into host BZT materials results in a complex reduction in the optical bandgap. Figure 5a presents UV–Vis absorption spectra of pure BZT and BZT- x Ni samples, indicating the modification of the absorption spectra of BZT compounds via random incorporation of Ni into the host lattice. The absorption spectra of pure BZT showed a single absorption edge with a shoulder, which was related to the surface defects and/or self-defects when samples were nanosized [3, 67–69]. Furthermore, as incorporating of Zr cations into BaTiO_3 to form $\text{BaTiO}_3\text{-BaZrO}_3$, one observed a shoulder in UV–Vis spectrum that presented a new local defect of Zr cations in the electronic structure of BaTiO_3 because of the zirconium $4d$ and titanium $3d$ states located below the conduction band [3, 68]. The bandgap decrease in BaTiO_3 via Zr incorporation was due to a structure symmetry break because of the presence of $[\text{ZrO}_6]$ cluster [70, 71]. Xin et al. reported that the optical band gap energy of BaTiO_3 compounds was dependent on Zr dopant concentration, where the large crystal splitting of the Zr $4d$ states was due to the deformation of the BZT crystal structure with increasing Zr amounts [72]. For Ni-doping BZT samples,

Fig. 5 **a** UV–Vis spectra and **b** plots of $(\alpha h\nu)^2$ values versus photon energy ($h\nu$) for the pure BZT and Ni-doped BZT compounds with various Ni concentrations. The inset of Fig. 5b shows the E_g values of the BZT compounds as a function of Ni impurity concentrations



the absorption spectroscopy of samples was modified, where the absorption edges of BZT compounds were distorted. Moreover, the double hump in the absorption spectroscopy was obtained in the absorption range of 600–900 nm with increasing intensity as the Ni concentration increased. This observation was well consistent with recent reports on the double humps in absorption spectra of Ni-doped lead-free ferroelectric materials, such as Ni-doped Bi_{0.5}K_{0.5}TiO₃ or Ni-doped Bi_{0.5}Na_{0.5}TiO₃ materials [22, 28, 52, 73, 74]. The double hump was related to a *3d*–*3d* interband transition of Ni cation's electron because of *3d* energy in octahedral under crystal field [20–22, 25–27, 29]. However, unlike the absorption spectra of Ni-doped Bi_{0.5}Na_{0.5}TiO₃ materials or Ni-doped Bi_{0.5}K_{0.5}TiO₃ materials, the absorption spectra of Ni-doped BZT materials indicated the presence of a shoulder in the range of 400–500 nm, as the Ni concentrations increased. The appearance of a shoulder and a hump in the absorption spectra of Ni-doped BZT materials was related to the presence of a multivalence state of Ni cations randomly incorporated at the *A* and *B* sites. By using Wood–Tauc relation between phonon energy $h\nu$ and bandgap E_g : $(\alpha h\nu) = A(h\nu - E_g)^n$, the optical bandgap E_g of studied samples was deduced, where n is a constant associated with different types of electronic transitions ($n = 2, 1/2, 3, \text{ or } 3/2$ or 3 for indirect allowed, direct allowed, indirect forbidden and direct forbidden transitions, respectively, and α is the absorption coefficient; A is a constant [75]. Thus, the E_g values of pure BZT compounds and Ni-doped BZT compounds were evaluated by extrapolating the linear portion of the curve or tail. Recently, Ba(Zr_{0.2}Ti_{0.8})O₃ compounds were reported to be direct allowed transition materials in Ref. [76]. As a result, in this study, the value $n = 1/2$ was used in the Wood–Tauc equation to obtain relation $(\alpha h\nu)^2$ proportional to photon energy ($h\nu$), as shown in Fig. 5b. The E_g values were then estimated by extrapolating the linear portion of the plot $(\alpha h\nu)^2$ versus $(h\nu)$ to $(\alpha h\nu)^2 = 0$. The estimation of E_g values for pure BZT compounds with the direct transition had values of 3.16 eV, which consisted of the recent observation from the first principle theoretical calculation for E_g values from 2.60 eV to 3.45 eV or was estimated from the experiment for E_g ranging from 2.92 eV to 3.84 eV, based on the amount of Zr dopants and method of fabrication [3, 68, 70–72, 76–78]. The addition of Ni impurities incorporated with the host BZT lattices resulted in the complex distortion of the E_g values, where the E_g value and Ni concentration changed from 3.23 to 3.14 eV and from 0.5 to 9 mol%, respectively, in BZT compounds. The inset in Fig. 5b shows in more detail the dependence of BZT's E_g values as a function of Ni doping concentration. The figure indicated that E_g values did not follow the trend recently reported in transition metal-doped lead-free ferroelectric materials [20–30]. In recent studies [20–29], we have suggested three main factors that affect the distortion

of the BZT's E_g values via incorporation of impurities: (i) appearance of a new local state in the middle of the bandgap of BZT compounds, (ii) creation of oxygen vacancies state locating below the conduction band, and (iii) lattice distortion caused by defects. By using theoretical DFT calculation, Ref. [49] predicted that, depending on density states, transition metal impurity atoms will incorporate with *A* sites or *B* sites of the lead-free ferroelectric perovskite structure. In Ref. [28], Thiet et al. reported the relation of the concentration of Ni cation incorporated into the host lattice and the decrease in E_g values in Ni-doped lead-free ferroelectric materials, whereas the phase segregated increased the E_g values. In this study, we observed a single perovskite phase of Ni-doped BZT compounds by XRD analysis. However, the possible phase segregation and Ni cations located at the interstitial site could not be detected by the XRD method. As a result, the complex variation in E_g values of BZT materials as a function of Ni concentrations needed further research. At least at present, the distortion of E_g values as a function of Ni impurity concentrations was confirmed by complex random incorporation of Ni with the host BZT lattices.

The observation in complex magnetic properties at room temperature of Ni-doped BZT materials was shown as a level of Ni doping concentrations. Figure 6 shows M–H loop curves of the pure BZT and BZT-xNi samples. The anti-S-shape of the pure BZT's M–H loop in Fig. 6a may be derived from the compensative interaction of diamagnetism with weak ferromagnetism as low saturation magnetization. The diamagnetic signal of the pure BZT material originated from empty states of *3d* orbital of Ti⁴⁺ cations [24, 29, 39, 79]. A typical M–H curve of pure BZT was obtained and is shown in the inset of Fig. 6a after subtracting the diamagnetic parts, which revealed the weak ferromagnetism property of pure BZT compounds. Figure 6a also exhibits a saturation magnetization M_s of 3.1 memu/g with nonzero remanent magnetization M_r of 0.4 memu/g and nonzero magnetic coercive field H_C of 0.98 Oe, confirming ferromagnetic ordering of the materials at RT. As mentioned in our previous studies [43–45], the weak ferromagnetism of pure BZT material at RT was related to surface effects and/or self-defects (e.g., Ti³⁺ defects and Ti⁴⁺ vacancies). The incorporation of Ni into the host BZT lattices enhanced the magnetic behavior. The diamagnetic signal of the BZT compounds was suppressed and the ferromagnetic signal was enhanced after doping Ni impurities (Fig. 6b–e). The opposite side observation for low Ni concentrations from 0.5 to 5 mol% is shown in Fig. 6b–e, which enhanced the ferromagnetic signal after introducing the Ni cation impurities. Positive and negative magnetization with the direction of the applied external magnetic field was obtained for 7 and 9 mol% Ni dopants, respectively (Fig. 6f, g). However, anti-S-shapes remained in the M–H curves as increasing Ni concentration up to 9 mol%. The results indicated that the ferromagnetic

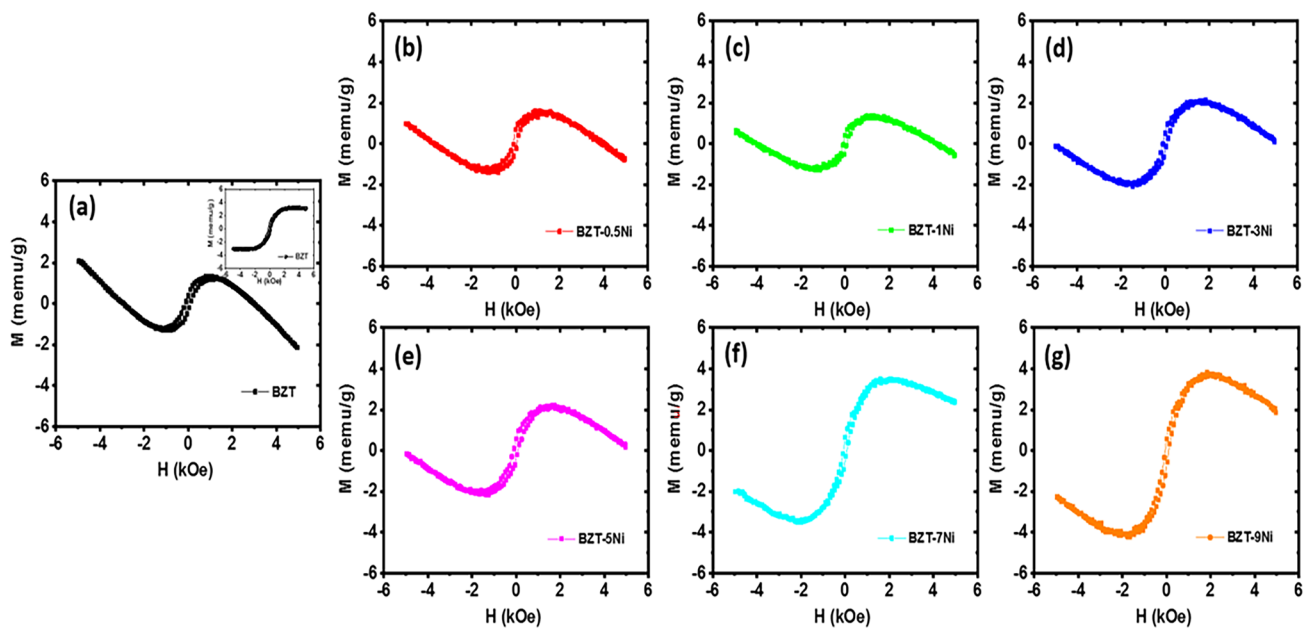


Fig. 6 Magnetic hysteresis loops at room temperature of **a** pure BZT and Ni-doped BZT compounds with various Ni concentrations: **b** 0.5, **c** 1, **d** 3, **e** 5, **f** 7, and **g** 9 mol%. The inset of Fig. 6 **a** shows the M - H curve of pure BZT compounds after extracting the diamagnetic part

properties of BZT materials were enhanced via the incorporation of Ni impurities compared with self-defect and/or surface effect induced (ferromagnetism in BZT). However, the Ni cations randomly incorporated with the host lattice BZT compound induced weak ferromagnetism, where the diamagnetic properties of samples were still affected by Ni-doped BZT samples. The weak ferromagnetic ordering at RT in Ni-doped lead-free ferroelectric materials in various families ($\text{Bi}_{0.5}\text{Na}_{0.5}\text{TiO}_3$, $\text{Bi}_{0.5}\text{K}_{0.5}\text{TiO}_3$, BaTiO_3 , or KNbO_3) was recently reported [22, 28, 37, 80].

To further understand the weak ferromagnetism in Ni-doped BZT materials, we introduced the possible spin configurations in Fig. 7. Notably, Ni cations possibly exist in

multivalence states, such as Ni^{2+} , Ni^{3+} , and Ni^{4+} states, where Ni^{2+} and Ni^{4+} cations could only be stable in a low spin state, whereas Ni^{3+} cations could be stable in both low and high spin states [50], as illustrated in Fig. 7 **a**–**c**, respectively. Consequently, if the magnetic moment was contributed only from the spin magnetic moment, then the spin moment of Ni^{2+} ($3d^84s^0$) cations in the spin configuration of $t_{2g}[\uparrow\downarrow\uparrow\downarrow\downarrow]e_g[\uparrow\uparrow]$ was $1 \mu_B/\text{Ni}$, and the spin moment of Ni^{4+} ($3d^64s^0$) cations in the spin configuration of $t_{2g}[\uparrow\downarrow\downarrow\downarrow\downarrow]e_g[\]$ was $0 \mu_B/\text{Ni}$. In addition, the spin moments of Ni^{3+} ($3d^74s^0$) cations in the low spin configuration of $t_{2g}[\uparrow\downarrow\downarrow\downarrow\downarrow]e_g[\uparrow]$ and in the high spin configuration of $t_{2g}[\uparrow\uparrow\uparrow\downarrow\downarrow]e_g[\uparrow\uparrow]$ were 0.5 and $1.5 \mu_B/\text{Ni}$, respectively. In Refs. [81–83], the authors

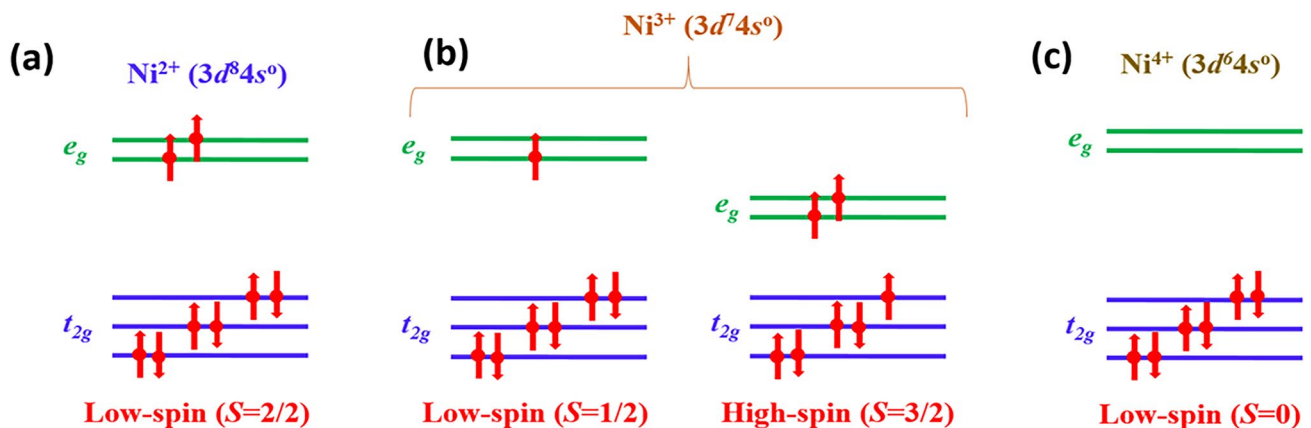


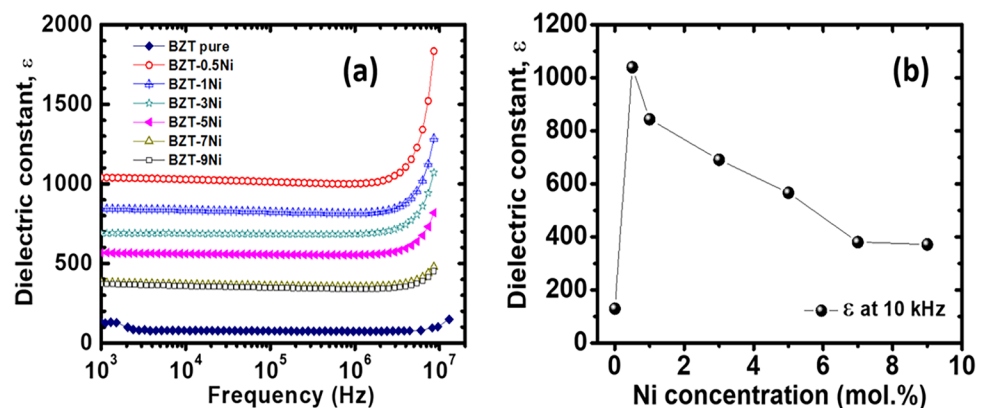
Fig. 7 Spin configuration of Ni cations located at the octahedral site because of the spin and valance states of **a** Ni^{2+} , **b** Ni^{3+} , and **c** Ni^{4+} cations

reported that an additional orbital might contribute to the magnetic moment of an ion through relaxation of orbital angular momentum quenching. This assumption seemed to be convincing because the magnetic moment decreased as increasing Ni amount due to an enhancement of quenching through increasing antiferromagnetic super-exchange coupling strength between two neighboring magnetic impurity ions via adjacent O²⁻ ions [52, 55]. Recently, Dung et al. reported that the possible Ni cations were more stable at a low spin state, resulting in a low magnetic moment [22]. The results were also consistent with the recent observation of the divalent state of Ni ions in Ni-doped Na_{0.5}Bi_{0.5}TiO₃ materials [84]. Consequently, based on the observation in the low magnetic moment of Ni-doped BZT compounds, we suggested that the original ferromagnetism ordering at RT in Ni-doped Na_{0.5}Bi_{0.5}TiO₃ was majorly originated from a low spin state interaction of Ni ion in Bi_{0.5}Na_{0.5}TiO₃ materials. However, the observation of nonzero H_C and M_r values in pure BZT and Ni-doped BZT compounds confirmed the presence of ferromagnetic states at RT. Consequently, the ferromagnetic properties are successfully combined in lead-free ferroelectric BZT materials.

To characterize the dielectric properties of studied samples, the dielectric constant was measured and is presented in Fig. 8a, b. As shown in Fig. 8a, the dielectric constant of each sample was almost a constant in the frequency range of 1 kHz–5 MHz, indicating a negligible effect of mobile charge carriers. In addition, the dielectric constant increased with frequency in the range of 5–13 MHz, which might relate to system resonance conditions [85]. We suggested that, at such high frequencies, the excess vibrations in the BZT materials promoted electronic polarization and resulted in the increase in the dielectric constant. The dielectric constant of pure BZT is about 80 ± 4 in the frequency range of 1 kHz–5 MHz. With doping 0.5 mol% Ni amounts, the dielectric constant of the material was strongly increased up to 1020 ± 10 , nearly 13 times higher than that of the pure BZT, as shown in Fig. 8b. However, the dielectric constant decreased monotonously with increasing Ni contents and

reached a saturated value of about 360 ± 10 . The dielectric constant of BZT-9Ni sample is still about four times higher than that of the pure PZT. The enhancement of dielectric constant possible resulted from electric heterogeneous nature and stronger polarization of perovskite structure by Ni doping. We suggested that the compression of BZT lattice parameters by Ni doping, as mentioned in the previous section, resulted in stronger polarization and subsequently caused the dielectric constant enhancement. According to Thakur et al. [85], the increase in dielectric constant with frequency at the high-frequency range for all studied samples might relate to system resonance conditions. Jie et al. reported that the dielectric properties of BZT materials were enhanced by Mn doping [86]. The enhanced dielectric behavior of BZT materials via Mn doping was suggested to cause by the compensation of the contribution of oxygen vacancy and the reorientation of defect complexes [86]. The dielectric properties of (Ba,Sr)TiO₃ materials were also reported to be enhanced via doping with Mn [87]. Li et al. reported that leakage current of (La,Fe)-co-doped Bi_{0.5}Na_{0.5}TiO₃-based materials was reduced; the ferroelectric and dielectric properties were enhanced, resulting from decreasing the carrier concentration by suppressing the oxygen vacancies, forming defect complex, and turning electron hopping through Ti⁴⁺ and Ti³⁺ via lattice distortion [88]. The defect complexes of Fe cations Fe_{Ti} and oxygen vacancies V_O , ($Fe_{Ti}V_OFe_{Ti}$) hindered the free movement of oxygen vacancies [89, 90]. Cai et al. reported that the dielectric constant of Ni-doped BZT ceramics was influenced by many factors such as crystallinity, grain size, and phase, where slightly doping of Ni strongly enhanced the dielectric constant [91]. In addition, Yan et al. reported that the dielectric constant of Fe-doped Ba(Zr_{0.1}Ti_{0.9})O₃ materials increased with decreasing compressive stresses and/or with increasing tensile stresses [92]. Our structural and microstructural studies on the Ni-doped BZT materials indicated that the lattice parameters tended to be compressed while the grain size was reduced as increasing the Ni doping concentrations. Therefore, at this moment, we could not conclude the main

Fig. 8 **a** Frequency dependence of dielectric constant, ϵ_r , of BZT and Ni-doped BZT samples with Ni concentration in the range of 0.5–9 mol%; **b** variation in dielectric constant measured at RT and 10 kHz frequency of Ni-doped BZT samples as a function of Ni concentration



reason for the observation of the complex dielectric properties of the Ni-doped BZT materials. Note that the natural defects of oxygen vacancies always existed in perovskite oxide materials. Thus, we suggested that low Ni concentrations exhibited defect complexes formed between Ni cations and natural defects of oxygen vacancies in BZT materials, e.g., $Ni_{Ti}V_O\dot{Ni}_{Ti}$, resulting in enhancement of the dielectric constant because of reduction of free electrons generated from oxygen vacancies. However, with further doping of Ni cations into the host BZT crystal, the oxygen vacancies were created and increased simultaneously with increasing the Ni concentrations because of unbalanced valence states between $Ni^{2+/3+}$ impurity cations substituted for Ti^{4+} cations. Increasing the amounts of oxygen vacancies and reduction in grain size as increasing the Ni concentrations in BZT materials led to decreasing the dielectric constant of BZT compounds as increasing the Ni concentrations. In addition, our X-ray diffraction studies on the influence of the Ni-doped BZT compounds showed that the lattice parameters of the BZT compounds tended to be compressed as increasing the Ni doping concentrations in BZT materials. The electron hopping between Ti^{3+} and Ti^{4+} cations was easier than that without doping. However, the defect complex between $Ni^{2+/3+}$ and oxygen vacancies ($Ni^{2+/3+}-V_O$) has dipole moment which could be oriented to align dipole along the direction of the applied electric field, resulting to would contribute to the dielectric process. As a result, the improvement in the dielectric constants in Ni-doped BZT materials overcomes by that of the pure BZT materials.

The influence of Ni doping amounts on the polarization of BZT materials as a function of the applied external electrical field was studied. Figure 9a–g shows

polarization–electric field hysteresis loops (P–E curves) of the pure BZT and BZT-xNi samples with $x=0.5, 1, 3, 5, 7,$ and 9 mol%, respectively, indicating unsaturation polarization under applied external electrical field at RT of all samples. The electrical remanent polarization (P_r) and coercive field (E_C) of the pure BZT compound were estimated at around $3.32 \mu\text{C}/\text{cm}^2$ and $0.59 \text{ kV}/\text{mm}$, respectively, which confirmed the natural ferroelectric property of BZT materials. With randomly incorporating Ni cations into the BZT host lattice, slim P–E curves were obtained and both P_r and E_C values were reduced. For the BZT-0.5Ni sample, the P_r and E_C values were decreased to $0.71 \mu\text{C}/\text{cm}^2$ and $0.36 \text{ kV}/\text{mm}$, respectively. For the BZT-9Ni sample, doped with 9 mol% Ni, the P_r and E_C values were estimated around $0.03 \mu\text{C}/\text{cm}^2$ and $0.05 \text{ kV}/\text{mm}$, respectively, indicating a strong reduction in the ferroelectric properties. The addition of Ni impurities into the host BZT compounds decreased the ferroelectric properties of the host BZT compounds, which were well understood via theoretical prediction [93]. Based on the first principle calculation for the compensative interaction between ferroelectric and ferromagnetic states in the perovskite structure, Hill et al. reported that the ferroelectric state required an empty $3d$ -orbital state for off-center distortion, while the ferromagnetic state was adapted for partially filling of electrons in the $3d$ orbital [93]. Consequently, the random distribution of Ni cations at Ti sites reduced the ferroelectric polarization and ferroelectric performance of the host BZT materials; the more the Ni doping, the slimmer the P–E hysteresis as shown in Fig. 8. Moreover, the unsaturation polarization shown in P–E curves of all studied samples was likely derived from surface

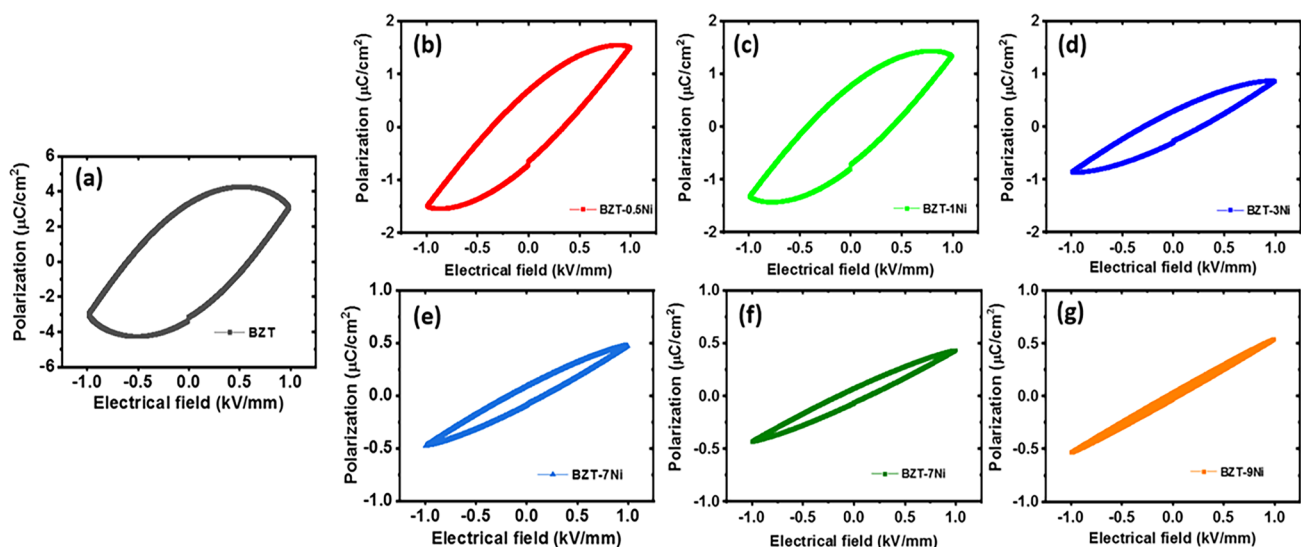


Fig. 9 Polarization hysteresis loops at room temperature of **a** pure BZT compounds and Ni-doped BZT with various levels of Ni dopants: **b** 0.5, **c** 1, **d** 3, **e** 5, **f** 7, and **g** 9 mol%

effect and impurity defects. Our microstructural study of the influence of Ni-doped BZT compounds showed that surface morphology was inhomogeneous at nano-size. The large surface area with defects induced low conductivity, thereby increasing the leakage current [94]. As a result, it was difficult to polarize the samples to a high electric field. By increasing the Ni concentrations, large amounts of oxygen vacancies were created via random incorporation of Ni^{2+/3+} with the Ti⁴⁺ sites, which exhibited large leakage currents in polarized samples at a high external electric field, resulting in unsaturation in the *P*–*E* hysteresis loop. Moreover, the crystal structure of BZT and Ni-doped BZT compounds indicated that the lattice parameter tended to shrink as the amount of Ni dopants increased. Therefore, we suggested that under an external electrical field, electron hopping between the Ti⁴⁺ ↔ Ti³⁺, Ni^{2+/3+} ↔ Ti³⁺, and/or Ni^{2+/3+} ↔ Ni^{2+/3+} was easier for Ni-doped BZT compounds than that between Ti⁴⁺ ↔ Ti³⁺ of pure BZT compounds, resulting in unsaturation and slim *P*–*E* hysteresis loops [95, 96]. The reduction in *P_r* and *E_C* values of BZT compounds by Ni doping indicated that the ferroelectric performance of BZT compounds decreased. However, the observation in non-rezo *P_r* and *E_C* values of BZT compounds doped up to 9 mol% Ni confirmed that ferroelectric remained but was weak. While the combination of multiferroic orders in one-phase materials is still a challenge in current research, our observations clearly showed stable ferroelectric properties at RT in the ferromagnetic state of Ni-doped BZT compounds.

4 Conclusions

To conclude, biferroic Ni-doped BZT compounds were successfully prepared via a chemical route. Self-defects and/or surface defects caused the weak ferromagnetism and compensated the natural diamagnetism in pure BZT compounds. The diamagnetism of BZT compounds tended to suppress the ferromagnetic state after Ni doping. The ferroelectric state of pure BZT compounds remained unchanged with the introduction of Ni impurity. The influence of surface defects and Ni defects reduced the BZT's ferroelectric performance. We hypothesized that both ferroic states of green ferroelectric Ni-doped BZT compounds could be used in novel smart electronic devices.

Acknowledgements This research is funded by The Ministry of Science and Technology, Viet Nam, under project number ĐTĐLCN.29/18 and this research was partially supported by the Ministry of Education and Training, Vietnam, under project number B2018-BKA-10-CtrVL.

Declaration

Conflict of interest The author(s) declare no competing interests.

References

- H. Wei, H. Wang, Y. Xia, D. Cui, Y. Shi, M. Dong, C. Liu, T. Ding, J. Zhang, Y. Ma, N. Wang, Z. Wang, Y. Sun, R. Wei, Z. Guo, *J. Mater. Chem. C* **6**, 12446–12467 (2018)
- WHO, Lead poisoning and health, 23 August 2019. <https://www.who.int/news-room/fact-sheets/detail/lead-poisoning-and-health>
- T. Badapanda, S.K. Rout, L.S. Cavalcante, J.C. Sczancoski, S. Panigrahi, E. Longo, M.S. Li, *J. Phys. D Appl. Phys.* **42**, 175414 (2009)
- D.E. Kotecki, J.D. Baniecki, H. Shen, R.B. Laibowitz, K.L. Saenger, J.J. Lian, T.M. Shaw, S.D. Athavale, C. Cabral, P.R. Duncombe, M. Gutsche, G. Kunkel, Y.J. Park, Y.Y. Wang, R. Wise, IBM, *J. Res. Dev.* **43**, 367–382 (1999)
- E. A. Fardin, K. Ghorbani, and A. S. Holland, *TENCON 2005 2005 IEEE Region 10*, 1–4 (2005).
- J. Jones, P. Zurcher, P. Che, D. Taylor, Y. Lii, B. Jiang, P. Maniar, S. Gillespie, *Microelectro. Eng.* **29**, 3–10 (1995)
- O. Auciello, S. Saha, D. Kaufman, S. Streiffer, W. Fan, B. Kabius, J. Im, P. Baumann, *J. Electroceram.* **12**, 119–131 (2004)
- A. Bootchanont, J. Jutimosik, S. Chandarak, M. Unruan, S. Rujirawat, R. Yimnirun, R. Guo, A. Bhalla, *Ceram. Inter.* **39**, S579–S582 (2013)
- J. Bera, S.K. Rout, *Mater. Lett.* **59**, 135–138 (2005)
- Z. Yu, R. Guo, A.S. Bhalla, *J. Appl. Phys.* **88**, 410–415 (2000)
- Z. Yu, C. Ang, R. Guo, A.S. Bhalla, *J. Appl. Phys.* **92**, 1489–1493 (2002)
- S. Mahajan, O.P. Thakur, C. Prakash, K. Sreenivas, *Bull. Mater. Sci.* **34**, 1483–1489 (2011)
- X.D. Huang, J.K.O. Sin, P.T. Lai, *IEEE Electron Dev. Lett.* **34**, 499–501 (2013)
- L. Liu, S. Ren, J. Zhang, B. Peng, L. Fang, D. Wang, *J. American Ceram. Soc.* **101**, 2408–2416 (2018)
- M. Veith, S. Mathur, N. Leckerf, V. Huch, T. Decker, *J. Sol gel Sci. Tech.* **15**, 145–158 (2000)
- D. Milicevic, K. Nikolic, J. Vukmirovic, N. Samardzic, V. V. Srdic, and G. Stojanovic, (2020) Resistive switching and synaptic behavior in zirconium doped thin film metal-oxide-metal devices. In: 23rd International Symposium on Design and Diagnostics of Electronic Circuits and Systems (DDECS). Doi: <https://doi.org/10.1109/DDECS50862.2020.9095643>.
- N.A. Spaldin, R. Ramesh, *Nature Mater.* **18**, 203–212 (2019)
- S. Shevlin, *Nature Mater.* **18**, 191–192 (2019)
- M.M. Vopson, *J. Crit. Rev. Solid State Mater. Sci.* **40**, 223–250 (2015)
- D.D. Dung, N.B. Doan, N.Q. Dung, N.H. Linh, L.H. Bac, L.T.H. Thanh, N.N. Trung, N.V. Duc, L.V. Cuong, D.V. Thiet, S. Cho, *J. Supercond. Novel Magn.* **32**, 3011–3018 (2019)
- D.D. Dung, N.B. Doan, N.Q. Dung, L.H. Bac, N.H. Linh, L.T.H. Thanh, D.V. Thiet, N.N. Trung, N.C. Khang, T.V. Trung, N.V. Duc, *J. Sci.: Adv. Mater. Dev.* **4**, 584–590 (2019)
- D.D. Dung, N.Q. Dung, N.B. Doan, N.H. Linh, L.H. Bac, N.N. Trung, N.V. Duc, L.T.H. Thanh, L.V. Cuong, D.V. Thiet, S. Cho, *J. Supercond. Novel Magn.* **33**, 911–920 (2020)
- L.T.H. Thanh, N.B. Doan, L.H. Bac, D.V. Thiet, S. Cho, P.Q. Bao, D.D. Dung, *Mater. Lett.* **186**, 239–242 (2017)

24. L.T.H. Thanh, N.B. Doan, N.Q. Dung, L.V. Cuong, L.H. Bac, N.A. Duc, P.Q. Bao, D.D. Dung, *J. Electron. Mater.* **46**, 3367–3372 (2017)
25. D.D. Dung, D.V. Thiet, D. Odkhuu, L.V. Cuong, N.H. Tuan, S. Cho, *Mater. Lett.* **156**, 129–133 (2015)
26. L.V. Cuong, N.H. Tuan, D. Odkhuu, D.V. Thiet, N.H. Dung, L.H. Bac, D.D. Dung, *Appl. Phys. A* **123**, 563 (2017)
27. N.H. Tuan, D.V. Thiet, D. Odkhuu, L.H. Bac, P.V. Binh, D.D. Dung, *Phys. B* **532**, 108–114 (2018)
28. D.V. Thiet, D.D. Cuong, L.H. Bac, L.V. Cuong, H.D. Khoa, S. Cho, N.H. Tuan, D.D. Dung, *Mater. Trans.* **56**, 1339–1343 (2015)
29. N.H. Tuan, V.K. Anh, N.B. Doan, L.H. Bac, D.D. Dung, D. Odkhuu, *J. Sol gel Sci. Tech.* **87**, 528–536 (2018)
30. J.A. Astudillo, S.A. Dionizio, J.L. Izquierdo, O. Moran, J. Heiras, G. Bolanos, *AIP Adv.* **8**, 055817 (2018)
31. D. Nie, J. Zhang, W.J. Deng, X. Chen, Z.Q. Mao, L.Y. Tang, *Chinese. J. Chem. Phys.* **30**, 97–102 (2017)
32. M. Manikandan, C. Venkateswaran, *AIP Conf. Proc.* **1665**, 130036 (2015)
33. I.S. Golovina, B.D. Shanina, S.P. Kolesnik, I.N. Geifman, A.A. Andriiko, *J. Appl. Phys.* **114**, 174106 (2013)
34. R.P. Tiwari, B. Birajdar, *AIP Conf. Proc.* **1942**, 030014 (2018)
35. B. Deka, S. Ravi, A. Perumal, D. Pamu, *Phys. B* **448**, 204–206 (2014)
36. S. Ray, Y.V. Kolenko, K.A. Kovnir, O.I. Lebedev, S. Turner, T. Chakraborty, R. Erni, T. Watanabe, G.V. Tendeloo, M. Yoshimura, *Nanotechnology* **23**, 025702 (2012)
37. S.K. Das, R.N. Mishra, B.K. Roul, *Solid State Communi.* **191**, 19–24 (2014)
38. X. Tong, Y.H. Lin, S. Zhang, Y. Wang, C.W. Nan, *J. Appl. Phys.* **104**, 066108 (2008)
39. J. Shah, R.K. Kotnala, *J. Mater. Chem. A* **1**, 8601–8608 (2013)
40. J.Y. Son, J.H. Lee, S. Song, Y.H. Shin, H.M. Jang, *ACS Nano* **7**, 5522–5529 (2013)
41. I.A. Starkov, G. Suchaneck, A.S. Starkov, G. Gerlach, *Ferroelectrics* **556**, 8–15 (2020)
42. Y. Zhang, H. Sun, W. Chen, *J. Phys. Chem. Solids* **114**, 207–219 (2018)
43. D.D. Dung, N.Q. Huy, N.H. Tuan, N.D. Quan, L.T. Lan, N.H. Linh, N.H. Thoan, N.N. Trung, L.H. Bac, *Mater. Lett.* **283**, 128897 (2021)
44. D.D. Dung, N.H. Tuan, C.T.T. Trang, N.Q. Huy, L.H. Bac, N.N. Thoan, N.D. Quan, N.N. Trung, N.H. Linh, *Appl. Phys. A* **127**, 61 (2021)
45. D.D. Dung, N.H. Tuan, N.D. Quan, N.Q. Huy, C.T.T. Trang, N.H. Thoan, N.N. Trung, N.T. Trang, L.H. Bac, *Res. Phys.* **19**, 103535 (2020)
46. D.D. Dung, N.T. Hung, D. Odkhuu, *Sci. Rep.* **9**, 18186 (2019)
47. D.D. Dung, N.T. Hung, *Appl. Phys. A* **126**, 240 (2020)
48. N.H. Tuan, L.H. Bac, L.V. Cuong, D.V. Thiet, T.V. Tam, D.D. Dung, *J. Electron. Mater.* **46**, 3472–3478 (2017)
49. D.D. Dung, N.Q. Dung, M.M. Hue, N.H. Lam, L.H. Bac, L.T.K. Phuong, N.N. Trung, D.D. Tuan, N.D. Quan, D. Sangaa, D. Odkhuu, *Vacuum* **179**, 109551 (2020)
50. R.D. Shannon, *Acta. Cryst. A* **32**, 751–767 (1976)
51. C. Chatzichristodoubou, P. Norby, P.V. Hendriksen, M.B. Mogensen, *J. Electroceram.* **34**, 100–107 (2015)
52. Z. Chen, C. Yuan, X. Liu, L. Meng, S. Cheng, J. Xu, C. Zhou, J. Wang, G. Rao, *Mater. Sci. Semicond. Proc.* **115**, 105089 (2020)
53. U. Holzwarth, N. Gibson, *Nature Nanotech.* **6**, 534 (2011)
54. H. P. Klug, and L. E. Alexander, (1974) *X-Ray Diffraction Procedures*, 2nd edn., Chap. 9 Wiley, London.
55. J.I. Langford, A.J.C. Wilson, *J. Appl. Cryst.* **11**, 102–113 (1978)
56. T. Badapanda, V. Senthil, S. Panigrahi, S. Anwar, *J. Electroceram.* **31**, 55–60 (2013)
57. H. Hayashi, T. Nakamura, T. Ebina, *J. Phys. Chem. Solids* **74**, 957–962 (2013)
58. A. Scalabrin, A.S. Chaves, D.S. Shim, S.P.S. Porto, *Phys. Status Solidi B* **79**, 731–742 (1977)
59. M. Singh, B.C. Yadav, A. Ranjan, M. Kaur, S.K. Gupta, *Sen. Act. B* **241**, 1170–1178 (2017)
60. L.P. Campos, D.E.D. Drogue, R. Lavin, S. Fuentes, *J. Molec. Struct.* **1099**, 502–509 (2015)
61. V. Vinothini, B. Vaidhyanathan, J. Binner, *J. Mater. Sci.* **46**, 2155–2161 (2011)
62. A. Dixit, S.B. Majumder, P.S. Dobal, R.S. Katiyar, A.S. Bhalla, *Thin Solid Films* **447**, 284–287 (2004)
63. L. Ramajo, M. Reboredo, M. Castro, *Compos. A* **36**, 1267–1274 (2005)
64. V. Buscaglia, S. Tripathi, V. Petkov, M. Dapiaggi, M. Deluca, A. Gajović, Y. Ren, *J. Phys. Cond. Matter.* **26**, 065901 (2014)
65. J. Pokorný, U. Pasha, L. Ben, O. Thakur, D. Sinclair, I. Reaney, *J. Appl. Phys.* **109**, 114110 (2011)
66. R. Kumar, K. Asokan, S. Patnaik, B. Birajdar, *J. Alloys Compound.* **737**, 561–567 (2018)
67. L.H. Bac, L.T.H. Thanh, N.V. Chinh, N.T. Khoa, D.V. Thiet, T.V. Trung, D.D. Dung, *Mater. Lett.* **164**, 631–635 (2016)
68. L.S. Cavalcante, J.C. Sczancoski, F.S.D. Vicente, M.T. Frabro, M.S. Li, J.A. Varela, E. Longo, *J. Sol-Gel Sci. Technol.* **49**, 35–46 (2009)
69. Y. Umeda, K. Takano, T. Kojima, A. Kuwabara, H. Moriwake, *Jpn. J. Appl. Phys.* **51**, 09LE01 (2012)
70. L.S. Cavalcante, V.M. Longo, M. Zampieri, J.W.M. Espinosa, P.S. Pizani, J.R. Sambrano, J.A. Varela, E. Longo, M.L. Simões, C.A. Paskocimas, *J. Appl. Phys.* **103**, 063527 (2008)
71. A. Kheyrdan, H. Abdizadeh, A. Shakeri, M.R. Golobostanfard, *J. Sol Gel Sci. Tech.* **86**, 141–150 (2018)
72. J.Z. Xin, C.W. Leung, H.L.W. Chan, *Thin Solid Films* **519**, 6313–6318 (2011)
73. M.M. Hue, N.Q. Dung, N.N. Trung, L.H. Bac, L.T.K. Phuong, N.V. Duc, D.D. Dung, *Appl. Phys. A* **124**, 588 (2018)
74. D.D. Dung, M.M. Hue, N.Q. Dung, L.T.K. Phuong, L.H. Bac, N.X. Duong, P.D. Luong, N.A. Duc, N.N. Trung, N.H. Thoan, D. Odkhuu, *Vacuum* **177**, 109306 (2020)
75. D.L. Wood, J. Tauc, *Phys. Rev. B* **5**, 3144 (1972)
76. G. Suchaneck, E. Chernova, A. Kleiner, R. Liebschner, L. Jastrabik, D.C. Mayer, A. Dejneka, G. Gerlach, *Thin Solid Films* **621**, 58–62 (2017)
77. Z.X. Yin, W.Y. Hua, Z. Min, Z. Na, G. Sai, C. Qiong, *Chin. Phys. Lett.* **28**, 067101 (2011)
78. S. Lee, R.D. Levi, W. Qu, S.C. Lee, C.A. Randall, *J. Appl. Phys.* **107**, 023523 (2010)
79. D.D. Dung, N.H. Lam, A.D. Nguyen, N.N. Trung, N.V. Duc, N.T. Hung, Y.S. Kim, D. Odkhuu, *Sci. Rep.* **11**, 8908 (2021)
80. B. Song, X. Wang, C. Xin, L. Zhang, B. Song, Y. Zhang, Y. Wang, J. Wang, Z. Liu, Y. Sui, J. Tang, *J. Alloys Compound.* **703**, 67–72 (2017)
81. S.B. Ogale, R.J. Choudhary, J.P. Buban, S.E. Lofland, S.R. Shinde, S.N. Kale, V.N. Kulkarni, J. Higgins, C. Lanci, J.R. Simson, N.D. Browning, S.D. Sarma, H.D. Drew, R.L. Greene, T. Venkatesan, *Phys. Rev. Lett.* **91**, 077205 (2003)
82. N.H. Hong, J. Sakai, A. Hassini, *Appl. Phys. Lett.* **84**, 2602–2604 (2004)
83. Y.R. Park, S.L. Choi, J.H. Lee, K.J. Kim, *J. Korean Phys. Soc.* **50**, 638–642 (2007)
84. S.K. Pradhan, S.K. De, *Ceram. Inter.* **44**, 15181–15191 (2018)
85. V.N. Thakur, B.P. Singh, S. Yadav, A. Kumar, *RSC Adv.* **10**, 9140–9145 (2020)
86. W.J. Jie, J. Zhu, W.F. Qin, X.H. Wei, J. Xiong, Y. Zhang, A. Bhalla, Y.R. Li, *J. Phys. D: Appl. Phys.* **40**, 2854–2857 (2007)

87. Z. Yuan, Y. Lin, J. Weaver, X. Chen, C.L. Chen, G. Subramanyam, J.C. Jiang, E.I. Meletis, *Appl. Phys. Lett.* **87**, 152901 (2005)
88. P. Li, W. Li, S. Liu, Y. Zhang, J. Zhai, H. Chen, *Ceram. Inter.* **41**, S344–S348 (2015)
89. M.M. Hejazi, E. Taghaddos, A. Safari, *J. Mater. Sci.* **48**, 3511–3516 (2013)
90. E. Aksel, E. Erdem, P. Jakes, J.L. Jones, R.d.A. Eichel, *Appl. Phys. Lett.* **97**, 012903 (2010)
91. W. Cai, J. Gao, C. Fu, L. Tang, *J. Alloys Compound.* **487**, 668–674 (2009)
92. S. Yan, Z. Zheng, Y. Li, W. Dun, Y. Wang, *Ceram. Inter.* **43**, 12605–12608 (2017)
93. N.A. Hill, *J. Phys. Chem. B* **104**, 6694–6709 (2000)
94. C. Mathieu, C. Lubin, G.L. Doueff, M. Cattelan, P. Gemeiner, B. Dkhil, E.K.H. Salje, N. Barrett, *Sci. Rep.* **8**, 13660 (2018)
95. Z. Pan, J. Chen, X. Jiang, Z. Lin, L. Zhang, L. Fan, Y. Rong, L. Hu, H. Liu, Y. Ren, X. Kuang, X. Xing, *Inorg. Chem.* **56**, 2589–2595 (2017)
96. E.V. Ramana, F. Figueiras, A. Mahajan, D.M. Tobaldi, B.F.O. Costa, M.P.F. Graca, M.A. Valente, *J. Mater. Chem. C* **4**, 1066–1079 (2016)

Publisher's Note Springer Nature remains neutral with regard to jurisdictional claims in published maps and institutional affiliations.